Green Chemistry

PAPER

View Article Online
View Journal | View Issue

Cite this: *Green Chem.*, 2020, **22**, 6540

Stabilization of Cu^+ by tuning a CuO–CeO_2 interface for selective electrochemical CO_2 reduction to ethylene†

Senlin Chu,‡[a] Xupeng Yan,‡[b] Changhyeok Choi,‡[c] Song Hong,[a] Alex W. Robertson,[d] Justus Masa,§[e] Buxing Han,[b] Yousung Jung *[c] and Zhenyu Sun *[a,f]

Electrochemical conversion of carbon dioxide (CO_2) into multi-carbon fuels and chemical feedstocks is important but remains challenging. Here, we report the stabilization of Cu^+ within a CuO–CeO_2 interface for efficient and selective electrocatalytic CO_2 reduction to ethylene under ambient conditions. Tuning the CuO/CeO_2 interfacial interaction permits dramatic suppression of proton reduction and enhancement of CO_2 reduction, with an ethylene faradaic efficiency (FE) as high as 50.0% at –1.1 V (*vs.* the reversible hydrogen electrode) in 0.1 M $KHCO_3$, in stark contrast to 22.6% over pure CuO immobilized on carbon black (CB). The composite catalyst presents a 2.6-fold improvement in ethylene current compared to that of CuO/CB at similar overpotentials, which also exceeds many recently reported Cu-based materials. The FE of C_2H_4 remained at over 48.0% even after 9 h of continuous polarization. The Cu^+ species are believed to be the adsorption as well as active sites for the activation of CO_2 molecules, which remain almost unchanged after 1 h of electrolysis. Further density functional theory calculations demonstrate the preferred formation of Cu^+ at the CuO–CeO_2 interface. This work provides a simple avenue to convert CO_2 into high-value hydrocarbons by rational stabilization of Cu^+ species.

Received 5th July 2020,
Accepted 1st September 2020

DOI: 10.1039/d0gc02279a

rsc.li/greenchem

Introduction

Electrochemical carbon dioxide (CO_2) reduction (ECR) shows promise in reducing greenhouse gas emissions, storing intermittent renewable electricity, as well as attaining energy security and sustainability.[1,2] Although this energy conversion process can be conducted under mild temperatures and atmospheric pressure, there are still many challenges, such as low conversion efficiency and poor product selectivity, which have to be overcome.[3,4] To enable progress towards this goal, the development of catalysts with high efficiency, sufficient selectivity, and low cost is necessary.[5,6] The synthesis of valuable hydrocarbons and other chemicals through ECR has drawn significant attention as a potential scheme for recycling CO_2.[7–18] In particular, C_{2+} (containing two or more carbon atoms) compounds such as ethylene have high energy densities and enjoy global demand in comparison to C_1 products.[19,20] For instance, ethylene is widely used as an industrial feedstock for manufacturing plastics and diesel, and its selective production in lieu of methane is important.

Copper, with its unique electronic properties, has been shown to stabilize CO intermediates (*CO) and enable them to be further reduced to multi-carbon products *via* CO dimerization to yield an *OCCO adsorbate and subsequent hydrogenations.[19] However, Cu is intrinsically limited by the scaling relations between the binding energies of various reaction intermediates on the metallic surfaces, which leads to wide product distributions and undesirable hydrogen evolution, thus hampering large-scale practical implementation.[21] Selective reduction of CO_2 into industrially important C_{2+} species remains an ongoing challenge. Recent investigations

[a]*State Key Laboratory of Organic-Inorganic Composites, Beijing University of Chemical Technology, Beijing 100029, China. E-mail: sunzy@mail.buct.edu.cn*
[b]*Beijing National Laboratory for Molecular Sciences, CAS Key Laboratory of Colloid and Interface and Thermodynamics, CAS Research/Education Center for Excellence in Molecular Sciences, Institute of Chemistry, Chinese Academy of Sciences, Beijing 100190, China*
[c]*Department of Chemical and Biomolecular Engineering, Korea Advanced Institute of Science and Technology (KAIST), Daejeon 34141, Republic of Korea. E-mail: ysjn@kaist.ac.kr*
[d]*Department of Materials, University of Oxford, Oxford, OX1 3PH, UK*
[e]*Analytische Chemie-Elektroanalytik & Sensorik, Ruhr University Bochum, D-44780 Bochum, Germany*
[f]*Key Laboratory of Low-Carbon Conversion Science & Engineering, Shanghai Advanced Research Institute, Chinese Academy of Sciences, China*

†Electronic supplementary information (ESI) available: Experimental details, XPS spectra, STEM images and EDS elemental maps, and FE *vs.* electrolysis temperature. See DOI: 10.1039/d0gc02279a

‡These authors contributed equally to this work.

§Current address: Max Planck Institute for Chemical Energy Conversion, Stiftstrasse 34–36, 45470 Mülheim an der Ruhr, Germany.

indicate that preferential conversion of CO_2 to C_{2+} products can be achieved using Cu-based materials doped with foreign atoms,[22] Cu alloys,[23,24] or through control of exposed crystal lattice,[25,26] oxidation state,[27,28] and surface morphology.[25,29–31] For example, single-crystal Cu(100) was demonstrated to display good selectivity for ethylene evolution with a faradaic efficiency (FE) of about 40.0%, which can be further improved to 50.0% over Cu(711) at 5.0 mA cm^{-2} in 0.1 M $KHCO_3$.[25] A recent study showed that CuAg bimetallic catalysts have enhanced selectivity to C_{2+} products, which was attributed to the suppression of the hydrogen evolution reaction (HER) due to the formation of compressively strained CuAg surface alloys.[32] In addition, Cu/oxide interfaces are regarded to be critical to inhibit the parasitic HER during electrocatalytic CO_2 reduction.[33,34] Oxides of copper exhibit enhanced ECR activity and increased selectivity towards multi-carbon products. The selectivity of these catalysts is dependent on the copper oxidation state.[31] Some computational studies have suggested that the coexistence of a Cu^+/Cu^0 mixture synergistically promotes CO_2 reduction to C_{2+} products due to improved CO_2 activation and CO dimerization.[35,36] Experimentally, however, evidence for the stability of the active Cu^+ species during CO_2 reduction remains unclarified thus far.

Herein, we report on the stabilization of Cu^+ by controlling the interplay between lattice-mismatched CuO and CeO_2. This scheme allows one to design an efficient and selective catalyst for electrocatalytic CO_2 reduction to produce ethylene, among other products (methane, carbon monoxide, formic acid, and ethanol). Catalytic selectivity can be greatly improved by taking advantage of the CuO–CeO_2 interactions in different composition regimes and interfacial structures. A remarkable FE for ethylene production of up to 50.0% was obtained at mild overpotentials, outperforming many previously reported Cu-based electrocatalysts. Furthermore, density functional theory (DFT) calculations revealed that CeO_2 changes the oxidation state of Cu atoms to Cu^+ at the CuO–CeO_2 interface.

Results and discussion

The X-ray diffraction (XRD) patterns of CuO–CeO_2/CB together with individual CuO/CB and CeO_2/CB are shown in Fig. 1a. Apart from a broad peak at 22.2° originating from carbon black with low crystallinity, diffraction peaks at about 28.1, 47.6, and 56.0° were observed in both CeO_2/CB and CuO–CeO_2/CB, corresponding to the (111), (220), and (311) planes of CeO_2 (PDF# 34-0394). These indicate the formation of fluorite ($Fm\bar{3}m$) CeO_2 with a face-centered cubic (fcc) structure in the composites. Unlike the bare CuO/CB that displayed representative monoclinic CuO peaks (PDF# 44-0706), no diffraction peaks of any Cu compounds were discernible in the XRD pattern of CuO–CeO_2/CB, likely due to the low loading and/or small size of CuO in the composite.

X-ray photoelectron spectroscopy (XPS) was used to acquire information about the surface composition and chemical state of the Cu species, as well as possible interactions between

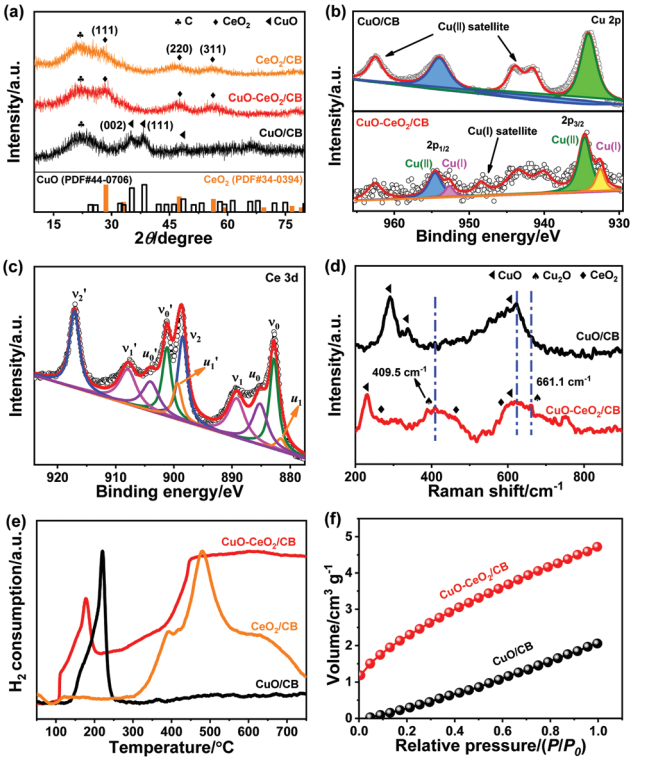

Fig. 1 (a) XRD patterns of CeO_2/CB, CuO/CB, and CuO–CeO_2/CB. (b) Cu 2p XPS spectra of CuO/CB and CuO–CeO_2/CB. (c) Ce 3d XPS spectrum of CuO–CeO_2/CB. (d) Raman spectra of CuO/CB and CuO–CeO_2/CB. (e) H_2-TPR profiles of CeO_2/CB, CuO/CB, and CuO–CeO_2/CB. (f) CO_2 adsorption isotherms of CuO/CB and CuO–CeO_2/CB.

copper and cerium oxides. Fig. 1b shows the Cu 2p signal of CuO/CB and CuO–CeO_2/CB. The Cu 2p core-level spectrum of CuO/CB reveals pronounced CuO features, that is, Cu $2p_{1/2}$ and $2p_{3/2}$ peaks with binding energies (BEs) at 954.0 and 934.0 eV, respectively. Strong Cu^{2+} satellites at 962.6, 944.0, and 941.6 eV were also clearly observed.[37] Nevertheless, no apparent peaks assigned to Cu^+ can be identified. In contrast, two peaks located at 954.3 and 951.9 eV were observed in CuO–CeO_2/CB, which can be attributed to Cu^{2+} $2p_{1/2}$ and Cu^+ $2p_{3/2}$, respectively.[10] This unambiguously verifies the formation and stabilization of Cu^+, likely owing to electron transfer from Ce^{3+} to Cu^{2+}. The relative Cu^+ percentage was determined to be 23.4% in CuO–CeO_2/CB, based on the peak area ratio of all copper oxidation states in the Cu 2p regions. Fig. 1c depicts the Ce 3d signals of CuO–CeO_2/CB having a satellite structure due to the hybridization of Ce 3d orbitals with O 2p orbitals and partial occupation of the 4f levels.[38] The $3d_{5/2}$ and $3d_{3/2}$ spin–orbit components (spin–orbit splitting, ~18.5 eV) are denoted as ν and ν', respectively, which is in line with the previous literature on Ce(IV).[39] The peaks of ν_0 and ν_1 were attributed to a mixing configuration of the $3d^9$ $4f^2$ (O $2p^4$) and $3d^9$ $4f^1$ (O $2p^5$) Ce^{4+} states and ν_2 to the $3d^9$ $4f^0$ (O $2p^6$) Ce^{4+} state.[38] The same assignment could be applied to the ν' structures, which correspond to the Ce $3d_{3/2}$ level. This illustrates the major valence of Ce(IV) in the sample, consistent with the

XRD result. Four peaks u_0 (BE ≈ 885.8 eV), u_1 (BE ≈ 880.6 eV), u_0' (BE ≈ 904.1 eV), and u_1' (BE ≈ 899.5 eV) associated with Ce^{3+} were identified, indicating the presence of Ce_2O_3 in the sample.[11] The well-defined peak ν_2' typical of Ce^{4+} can be used to estimate the fraction of Ce^{4+}.[40] Given that the area of the ν_2' component comprises 14.0% of the overall area of the Ce 3d region, the Ce^{3+} percentage was estimated to be 27.0%. The deconvoluted O 1s XPS spectrum of CuO–CeO_2/CB (Fig. S1a†) displays a predominant peak at 529.7 eV arising from the lattice oxygens in the metal oxides, and two less intense peaks at 531.2 and 532.6 eV that can be assigned to defective sites (surface oxygen vacancies) and physisorbed water, respectively.

The presence of Cu^+ in CuO/CeO_2 heterostructures was also evidenced by Raman scattering experiments. The bands centered at about 258.0, 462.9, and 595.0 cm^{-1} were identified as shown in Fig. 1d, which can be well assigned to the F_{2g} mode, second-order transverse acoustic (2TA) mode, and defect-induced (D) mode of fluorite CeO_2, respectively.[41] It is worth noting that the three peaks at 290.4, 337.0, and 622.8 cm^{-1} that appeared for CuO/CB are attributed to the respective single A_g mode and two B_g optical modes of cupric oxide.[42] However, for CuO–CeO_2/CB, the feature around 290.4 cm^{-1} disappeared and a new band at 230.4 cm^{-1} was observed being tentatively assigned to one-magnon scattering, which arose from the antiferromagnetic ordering of the Cu^{2+} ions.[42] Two additional distinct peaks at 409.5 and 661.1 cm^{-1} were observed that were typical of Cu^+ Raman fingerprints.[42] This further confirms that CuO was partially converted to Cu_2O, possibly induced by adjacent CeO_2 nanoparticles (NPs). These results are consistent with the XPS data in Fig. 1b.

Temperature-programmed reduction by hydrogen (H_2-TPR, Fig. 1e) manifested two marked H_2 consumption peaks at 110.0 and 178.0 °C for CuO–CeO_2/CB, which were ascribed to the reduction of the subsurface $Cu^{\delta+}$ to Cu^+ and further to Cu^0, respectively, by consuming reducible oxygen from the CuO_x species. Notably, the TPR reduction peaks shifted to lower temperatures relative to CuO/CB, which is likely a result of hydrogen spillover to CuO at the CuO/CeO_2 interface. Furthermore, CuO–CeO_2/CB exhibited a CO_2 uptake capacity of 4.7 $cm^3\ g^{-1}$ (Fig. 1f), 2.3 fold as large as that of CuO/CB. This could lead to enriched CO_2 on the local surface of the working electrode, thus boosting *CO coverage and dimerization. The significant enhancement in CO_2 capture ability is due to the introduction of CeO_2, which can effectively adsorb CO_2, forming carbonates and hydrogen carbonates.[43] It can be envisioned that the as-made hybrid catalyst may facilitate multiple interesting functionalities such as adsorption, electronics, activation, and catalysis, among others, based on the synergistic interaction between CuO and CeO_2.

To decipher the morphological features of our catalyst, aberration-corrected high-angle annular dark-field scanning transmission electron microscopy (HAADF-STEM) was performed on CuO–CeO_2/CB. Fig. 2a and b show the formation of many reticular NPs homogeneously distributed on carbon black. The (111) and (100) planes of CeO_2 were indexed with the aid of fast Fourier transformation (FFT) (inset of Fig. 2b).

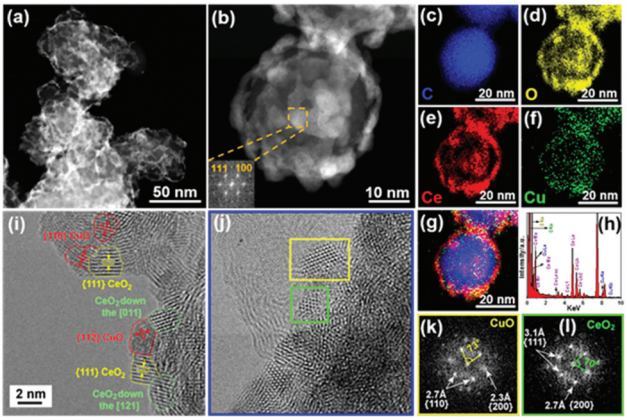

Fig. 2 (a and b) HAADF-STEM images of CuO–CeO_2/CB. The inset in image (b) shows the corresponding FFT of CuO–CeO_2/CB. EDS elemental maps of (c) C, (d) O, (e) Ce, (f) Cu, and (g) overlay of C (blue), Ce (red), and Cu (green) over the region shown in image (b), along with corresponding EDS spectrum (h). (i) HRTEM image of CuO–CeO_2/CB. (j–l) Magnified image of the blue rectangle in image (i) and FFTs of the regions encased by the yellow and green rectangles in image (j).

Furthermore, the energy-dispersive X-ray spectroscopy (EDS) maps (Fig. 2c–g and Fig. S2b–f†) along with the EDS spectrum (Fig. 2h) confirmed that the NPs were composed of CuO and CeO_2 crystallites. EDS elemental mapping revealed an almost full overlap of the Cu-rich and Ce-rich domains, indicating large interfaces between the two metal oxides. The crystallite sizes of CuO and CeO_2 were found to be similar with the sizes being less than 5 nm as found using high-resolution TEM (Fig. 2i and j). By FFT, the fcc CuO and CeO_2 NPs were discerned (Fig. 2k and l). Most of the CuO crystals exhibited a faceted cuboidal morphology and were surrounded by CeO_2 NPs (Fig. 2i and j).

ECR is very sensitive to operating conditions, such as the nature and properties of the electrocatalyst, electrolyte composition, and electrochemical cell type. To evaluate the intrinsic catalytic properties of the as-prepared hybrids, we conducted the ECR in CO_2-saturated 0.1 M $KHCO_3$ aqueous electrolyte (pH 6.8) using a reported design of liquid H-type cell with continuous CO_2 bubbling.[44] The potential-dependent geometric current densities of CuO–CeO_2/CB within the potential range of 0.0 to −1.4 V (*vs.* RHE) were recorded by linear sweep voltammetry (LSV), as shown in Fig. 3a. Significantly higher cathodic currents were observed in a CO_2 environment than in an Ar environment within the entire potential region. CO, H_2, CH_4, HCOOH, C_2H_4, and C_2H_5OH were detected at applied potentials ranging from −0.9 to −1.3 V (*vs.* RHE) in a CO_2-saturated 0.1 M $KHCO_3$ solution. The ECR preferably occurred over HER at potentials ranging from −0.9 to −1.2 V (*vs.* RHE), while HER dominated at more negative potentials (Fig. 3b and c). As demonstrated in Fig. 3d, CeO_2/CB generated exclusively H_2 with a very small amount of ECR products (FE < 3.0%). Commercial Cu_2O decorated on CB exhibited an FE of 31.7% for ECR (*vs.* RHE) (Fig. S3†), whereas the FE for C_2H_4 formation was as low as 8.5%. Although CuO/CB can reduce CO_2

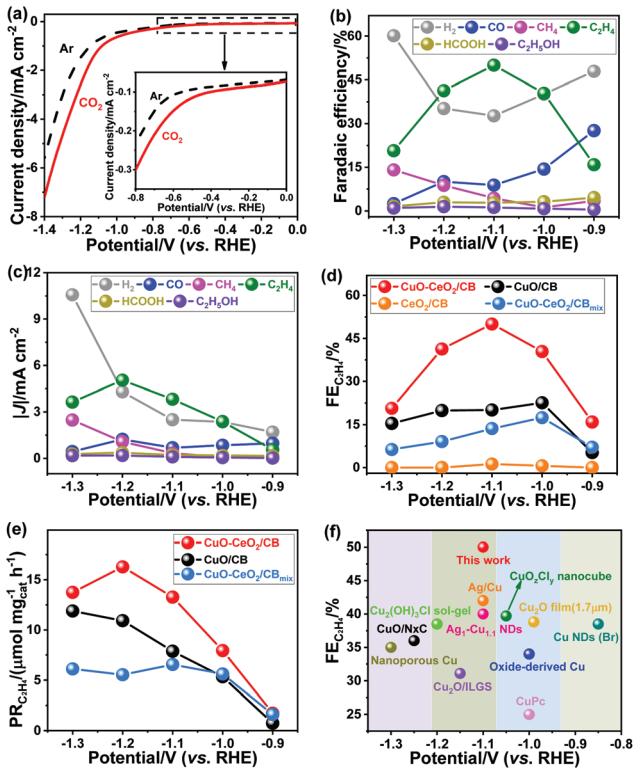

Fig. 3 (a) LSV results of CuO–CeO_2/CB on a glassy carbon electrode in Ar- (dashed black line) or CO_2 (solid red line)-saturated 0.1 M $KHCO_3$ solutions at a scan rate of 5 mV s^{-1}. (b) Faradaic efficiencies and (c) partial current densities for ECR products over CuO–CeO_2/CB at various applied potentials. (d) C_2H_4 FEs of CuO–CeO_2/CB, CuO/CB, CeO_2/CB, and CuO–CeO_2/CB_{mix} in the potential range from −0.9 to −1.3 V. (e) Production rates of C_2H_4 at different potentials over CuO–CeO_2/CB, CuO/CB, and CuO–CeO_2/CB_{mix}. (f) C_2H_4 FEs of CuO–CeO_2/CB and other reported Cu-based electrocatalysts.

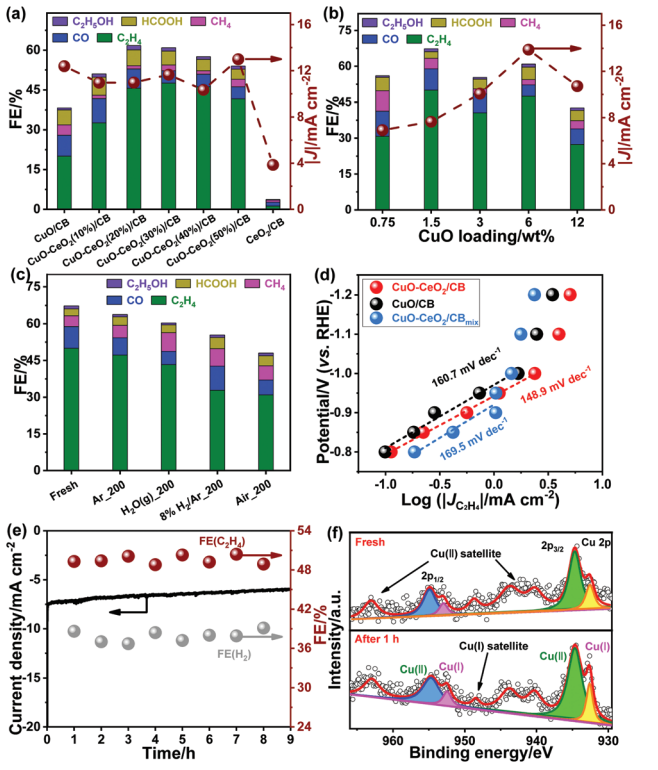

Fig. 4 FE and geometric current density at −1.1 V as a function of (a) CeO_2 loading at a fixed CuO content of 6.0 wt% and (b) CuO loading at a constant CeO_2 loading of 30.0 wt%. (c) FEs at −1.1 V over fresh and treated CuO–CeO_2/CB under Ar, H_2O, 8.0% H_2/Ar, and air. (d) Tafel plots of the partial geometric current density for C_2H_4 production over CuO–CeO_2/CB, CuO/CB, and CuO–CeO_2/CB_{mix}. (e) Geometric current-, C_2H_4 FE-, and H_2 FE-time responses of CuO–CeO_2/CB at −1.1 V. (f) Cu 2p XPS spectra of CuO–CeO_2/CB before and after 1 h of electrolysis.

at overpotentials larger than 0.97 V, the highest FE for ECR was below 32.0%, with the selectivity for C_{2+} products being less than 23.0%. It is worth noting that the CuO–CeO_2/CB nanocomposites substantially promoted the activity toward CO_2 reduction with an FE > 63.0%.

The C_1 products were obtained at similar yields for CuO/CB and CuO–CeO_2/CB, but C_{2+} product selectivity and C_2H_4 FE and production rate (Fig. 3e) were remarkably boosted for the latter sample. C_2H_4 emerged at an onset potential of −0.7 V (*vs.* RHE) over CuO–CeO_2/CB and rose to a maximum with FE up to 50.0% at −1.1 V (*vs.* RHE) in contrast to that of 22.6% and 1.2% for CuO/CB and CeO_2/CB, respectively (Fig. 3b and d). The C_2H_4 selectivity even outperforms many recently reported Cu-based electrocatalysts under similar overpotentials (Fig. 3f), such as the state-of-the-art Cu nanocubes with exposed (100) facets (maximum C_2H_4 FE is 32.0%)[45,46] and Ag–Cu nanodimers (maximum C_2H_4 FE is 40.0%).[24]

The ECR activity was tunable by adjusting the amounts of CeO_2 and CuO (Tables S1 and S2†). As seen in Fig. 4a, incorporation of CeO_2 at various amounts was found to thwart hydrogen evolution and facilitate C_2H_4 generation. The optimal loading of CeO_2 was 30.0 wt%. A continuous increase in CeO_2 loading led to a slight decrease in ECR activity, probably owing to the reduction in electrical conductivity. Likewise, the ECR activity to yield C_2H_4 increased with the mass percentage of CuO in the range of 0.75–1.5 wt%. The C_2H_4 FE tended to diminish upon a further increase in CuO loading (Fig. 4b). This may be due to a combination of the less extended interface and formation of larger CuO particles, resulting in weakened binding of the reactants and intermediates. Furthermore, it was found that there is an optimum in the particle size of CuO, which maximized C_2H_4 generation (Table S3†), in line with the results observed for Cu in the literature.[24] The effect of electrolytic temperature on ECR was also explored. The FE for ECR was found to be maximized at 3 ± 3 °C (Fig. S4†), indicating that the HER tends to be inhibited at low reaction temperatures.

To check whether Ce^{3+} impacted the ECR, the synthesis of catalysts was performed in an air-free glove-box under otherwise similar conditions. The resulting CuO–Ce_2O_3/CB provided a much lower C_2H_4 FE (22.4% at −1.1 V *vs.* RHE) compared to CuO–CeO_2/CB. This indicates that Ce^{3+} is unlikely to contribute to the enhanced ECR.

The role of Cu^+ during ECR was investigated by treating CuO–CeO_2/CB at 200 °C under different atmospheres. The relative fractions of Cu^0, Cu^+, and Cu^{2+} in the treated CuO–CeO_2/CB samples were probed using XPS (Table S4 and Fig. S5†). As observed in Fig. 4c, the CO_2 reduction activity and selectivity dropped slightly in an Ar environment, which may favor the transformation of a small fraction of Cu^{2+} to Cu^+ and Cu^+ to Cu^0 (Table S4 and Fig. S5a†). The C_2H_4 FE mildly decreased with a simultaneous increase in CH_4 FE, probably resulting from the aggregation of metal oxide NPs and the presence of Cu^0. This phenomenon became a little more pronounced after being subjected to water vapor, which may be due to the promotion of CH_4 formation by the adsorbed surface water molecules, in addition to the transformation of Cu^+ (Table S4 and Fig. S5b†). However, annealing of the catalyst in 8% H_2/Ar led to increased HER with a distinct drop in ECR performance. Despite CO FE being improved to 33.7%, the C_2H_4 FE dropped to 33.8%. This suggests that the reduction of Cu^+/Cu^0 ratio (Table S4 and Fig. S5c†) is detrimental to CO–CO coupling. In addition, the decrease in Cu^+/Cu^{2+} (Table S4 and Fig. S5d†) upon exposure of the sample to air at elevated temperatures degraded C_2H_4 production, accompanied by substantially more H_2 evolution.

To probe the role of the CuO–CeO_2 interface, we made efforts to tailor the interfacial structure by fine-tuning synthetic parameters such as the feeding sequence of metal precursors. When the precursor $Cu(Ac)_2$ was first added followed by the addition of $Ce(NO_3)_3$ to prepare the catalyst, only 22.0% of C_2H_4 FE was attained (Table S5†). Alternatively, a cascade addition of cerium precursor and copper precursor in sequence also increased C_2H_4 FE only to about 37.8%. In both cases, the accessible CuO–CeO_2 interfaces with exposed copper domains were markedly reduced, which accounted for the declined ECR performance. A physical mixture of CuO/CB and CeO_2/CB (CuO–CeO_2/CB_{mix}) with equivalent metal oxide loadings was also evaluated for ECR. It showed even worse CO_2 reduction activity than that of CuO/CB (Fig. 3d and e), most likely due to poor mass transport. Taken together, we conclude that an intelligent design of CuO–CeO_2 interfaces to yield and stabilize Cu^+ is essential to facilitate the CO_2-to-C_2H_4 conversion.

The interfacial reaction kinetics was explored by Tafel analysis. A Tafel slope of 148.9 mV dec^{-1} was observed for CuO–CeO_2/CB, much lower than 160.7 mV dec^{-1} for CuO/CB and 169.5 mV dec^{-1} for CuO–CeO_2/CB_{mix} (Fig. 4d). This indicates that CuO–CeO_2/CB has a comparatively faster kinetics for CO_2 reduction. The formation of the *CO intermediate for tandem catalysis on the surface of the catalysts determines the reaction rate.

The long-term performances of the catalysts were examined by chronoamperometric measurements. The results (Fig. 4e) showed that the FE for C_2H_4 remained steady, exceeding 48.0% even after 9 h of continuous polarization at −1.1 V (*vs.* RHE). XPS analysis (Fig. 4f and S1b†) indicated that the surface concentration of Cu^+ was preserved after 1 h of polarization at −1.1 V (*vs.* RHE), reflecting its good stability owing to the strong interplay between ceria and copper oxide.

To further investigate the role of CeO_2 in stabilizing Cu^+, we performed density functional theory (DFT) calculations (Fig. 5). We modeled the interface between CuO and CeO_2 (denoted as CuO–CeO_2) by constructing a small CeO_2 cluster (Ce_3O_6) on the CuO(100) surface.[47,48] The (100) facet, which has been known as the active site for C_2 production in electrochemical CO_2 reduction, is considered.[49] We also considered the Cu-terminated surface of CuO since the surface O species would be reduced at the experimental electrode potential range (−0.9 ~ −1.3 V *vs.* RHE). Previous studies have shown that subsurface oxygen in copper oxides plays an important role in facilitating the CO_2 reduction,[35,36] and hence, we focus on subsurface O rather than surface O.

We focused on the change/trend of the Bader charges[50] of the surface Cu atoms with and without CeO_2 clusters since the Bader charge agrees with the oxidation state qualitatively (albeit not quantitatively). Assuming that the Bader charges of surface Cu atoms in Cu(100), Cu_2O(100), and CuO(100) correspond to the oxidation states of 0, +1, and +2, respectively, we obtained a linear relationship between the Bader charge and oxidation state (Fig. 5d), and from the latter correlation, we obtained the oxidation state of Cu atoms in CuO–CeO_2.

This Bader charge analysis shows that the oxidation states of several Cu atoms at the CuO–CeO_2 interface lie between that of Cu_2O and CuO (Fig. 5d), indicating that the interfacial CeO_2 cluster changes the oxidation state of neighboring Cu atoms in CuO toward that of Cu_2O. More specifically, the oxidation states of two Cu atoms at the CuO–CeO_2 interface are highly similar to those of surface Cu atoms in Cu_2O (*i.e.* Cu^+). This result agrees with the presence of Cu^+ in the XPS characterization of CuO–CeO_2/CB (Fig. 1b), and indicates that CeO_2 plays an important role in stabilizing Cu^+.

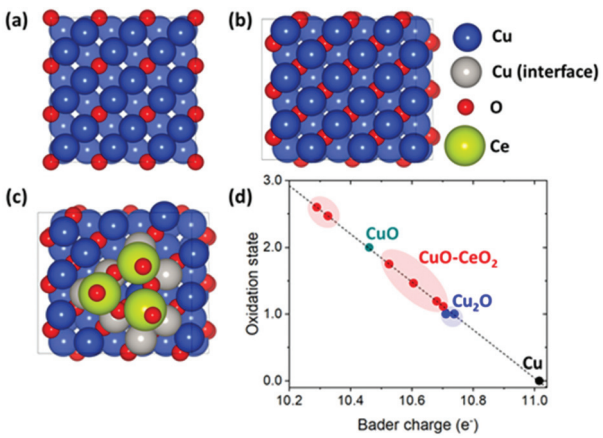

Fig. 5 Top view of the optimized geometries of (a) Cu_2O, (b) CuO, and (c) CuO–CeO_2. (d) Oxidation states of surface Cu atoms obtained by Bader charge analysis. Only the surface Cu atoms adjacent to CeO_2 (denoted as grey balls in (c)) are considered for the Bader charge analysis of CuO–CeO_2. In (d), black, blue, cyan, and red colors represent Cu, Cu_2O, CuO, and CuO–CeO_2, respectively.

Conclusions

In summary, we present CuO–CeO_2/CB as a highly promising electrocatalyst for enhancing the selective reduction of CO_2 to ethylene. By utilizing the strong synergistic interaction between CuO and CeO_2, stabilization of the Cu^+ species at the metal–oxide interface is realized, while H_2 production is simultaneously considerably suppressed, resulting in boosted ethylene production with a high FE of up to 50.0%. The existence of Cu^+ species was confirmed by XPS, Raman spectroscopy, as well as TPR; Cu^+ species are believed to be the adsorption as well as active sites for the activation of CO_2 molecules. This work provides a simple way to enhance the conversion of CO_2 into ethylene, and it is hoped that the findings will inspire the rational design of active copper domains for efficient electroreduction of CO_2.

Conflicts of interest

The authors declare no conflicts of interest.

Acknowledgements

This work was supported by the National Natural Science Foundation of China (No. 21972010); the State Key Laboratory of Organic-Inorganic Composites (No. oic-201901001); the Beijing Natural Science Foundation (No. 2192039); the Beijing University of Chemical Technology (XK180301 and XK1804-2); the Foundation of Key Laboratory of Low-Carbon Conversion Science & Engineering, Shanghai Advanced Research Institute, the Chinese Academy of Sciences (No. KLLCCSE-201901, SARI, CAS); the DCCEM at the Department of Materials, Oxford University, and the the Henry Royce Institute (EP/R010145/1). Y. J. acknowledges the National Research Foundation of Korea (NRF-2019M3D1A1079303 and NRF-2019M3D3A1A01069099).

Notes and references

1 J. Gu, C. Hsu, L. Bai, H. Chen and X. Hu, *Science*, 2019, **364**, 1091–1094.
2 S. Nitopi, E. Bertheussen, S. B. Scott, X. Liu, A. K. Engstfeld, S. Horch, B. Seger, I. E. L. Stephens, K. Chan, C. Hahn, J. K. Nørskov and I. Chorkendorff, *Chem. Rev.*, 2019, **119**, 7610–7672.
3 Z. Sun, T. Ma, H. Tao, Q. Fan and B. Han, *Chem*, 2017, **3**, 560–587.
4 T. Ma, Q. Fan, X. Li, J. Qiu, T. Wu and Z. Sun, *J. CO2 Util.*, 2019, **30**, 168–182.
5 H. Tao, Q. Fan, T. Ma, S. Liu, H. Gysling, J. Texter, F. Guo and Z. Sun, *Prog. Mater. Sci.*, 2020, 100637.
6 Q. Fan, P. Hou, C. Choi, T. S. Wu, S. Hong, F. Li, Y. L. Soo, P. Kang, Y. Jung and Z. Sun, *Adv. Energy Mater.*, 2020, **10**, 1903068.
7 A. Guan, Z. Chen, Y. Quan, C. Peng, Z. Wang, T.-K. Sham, C. Yang, Y. Ji, L. Qian and X. Xu, *ACS Energy Lett.*, 2020, **5**, 1044–1053.
8 Y. Pi, J. Guo, Q. Shao and X. Huang, *Nano Energy*, 2019, **62**, 861–868.
9 H. Yang, Y. Wu, G. Li, Q. Lin, Q. Hu, Q. Zhang, J. Liu and C. He, *J. Am. Chem. Soc.*, 2019, **141**, 12717–12723.
10 J. Lv, M. Jouny, W. Luc, W. Zhu, J. Zhu and F. Jiao, *Adv. Mater.*, 2018, **30**, 1803111.
11 M. Jia, C. Choi, T. Wu, C. Ma, P. Kang, H. Tao, Q. Fan, S. Hong, S. Liu, Y. Soo and Z. Sun, *Chem. Sci.*, 2018, **9**, 8775–8780.
12 M. Jia, Q. Fan, S. Liu, J. Qiu and Z. Sun, *Curr. Opin. Green Sustainable Chem.*, 2019, **16**, 1–6.
13 S. Liu, X. Lu, J. Xiao, X. Wang and X. Lou, *Angew. Chem. Int. Ed.*, 2019, **58**, 13828–13833.
14 Q. Gong, P. Ding, M. Xu, X. Zhu, M. Wang, J. Deng, Q. Ma, N. Han, Y. Zhu and J. Lu, *Nat. Commun.*, 2019, **10**, 1–10.
15 C. Xia, P. Zhu, Q. Jiang, Y. Pan, W. t. Liang, E. Stavitsk, H. N. Alshareef and H. Wang, *Nat. Energy*, 2019, **4**, 776–785.
16 D. Gao, H. Zhou, F. Cai, J. Wang, G. Wang and X. Bao, *ACS Catal.*, 2018, **8**, 1510–1519.
17 Z. Liu, *Acta Phys.-Chim. Sin.*, 2019, **35**, 1307–1308.
18 Y. Yang, Y. Zhang, J. Hu and L. Wan, *Acta Phys.-Chim. Sin.*, 2020, **36**, 1906085–1906080.
19 Q. Fan, M. Zhang, M. Jia, S. Liu, J. Qiu and Z. Sun, *Mater. Today Energy*, 2018, **10**, 280–301.
20 Y. Gao, S. Liu, Z. Zhao, H. Tao and Z. Sun, *Acta Phys.-Chim. Sin.*, 2018, **34**, 858–872.
21 T. Ma, Q. Fan, H. Tao, Z. Han, M. Jia, Y. Gao, W. Ma and Z. Sun, *Nanotechnology*, 2017, **28**, 472001–472019.
22 Y. Zhou, F. Che, M. Liu, C. Zou, Z. Liang, P. De Luna, H. Yuan, J. Li, Z. Wang and H. Xie, *Nat. Chem.*, 2018, **10**, 974–980.
23 A. Vasileff, C. Xu, Y. Jiao, Y. Zheng and S.-Z. Qiao, *Chem*, 2018, **4**, 1809–1831.
24 J. Huang, M. Mensi, E. Oveisi, V. Mantella and R. Buonsanti, *J. Am. Chem. Soc.*, 2019, **141**, 2490–2499.
25 Y. Hori, I. Takahashi, O. Koga and N. Hoshi, *J. Mol. Catal. A: Chem.*, 2003, **199**, 39–47.
26 Y. A. Wu, I. McNulty, C. Liu, K. C. Lau, Q. Liu, A. P. Paulikas, C.-J. Sun, Z. h. Cai, J. R. Guest and Y. Ren, *Nat. Energy*, 2019, **4**, 957–968.
27 S. Y. Lee, H. Jung, N. K. Kim, H. S. Oh, B. K. Min and Y. J. Hwang, *J. Am. Chem. Soc.*, 2018, **140**, 8681–8689.
28 H. Jung, S. Y. Lee, C. W. Lee, M. K. Cho, D. H. Won, C. Kim, H.-S. Oh, B. K. Min and Y. J. Hwang, *J. Am. Chem. Soc.*, 2019, **141**, 4624–4633.
29 W. Luc, X. Fu, J. Shi, J.-J. Lv, M. Jouny, B. H. Ko, Y. Xu, Q. Tu, X. Hu and J. Wu, *Nat. Catal.*, 2019, **2**, 423–430.
30 D.-H. Nam, O. S. Bushuyev, J. Li, P. De Luna, A. Seifitokaldani, C.-T. Dinh, F. P. García de Arquer, Y. h. Wang, Z. q. Liang and A. H. Proppe, *J. Am. Chem. Soc.*, 2018, **140**, 11378–11386.

31 P. De Luna, R. Quintero-Bermudez, C. T. Dinh, M. B. Ross, O. S. Bushuyev, P. Todorović, T. Regier, S. O. Kelley, P. d. Yang and E. H. Sargent, *Nat. Catal.*, 2018, **1**, 103–110.
32 E. L. Clark, C. Hahn, T. F. Jaramillo and A. T. Bell, *J. Am. Chem. Soc.*, 2017, **139**, 15848–15857.
33 S. Chu, S. Hong, J. Masa, X. Li and Z. Sun, *Chem. Commun.*, 2019, **55**, 12380–12383.
34 Y. Li, S. Chu, H. Shen, Q. Xia, A. W. Robertson, J. Masa, U. Siddiqui and Z. Sun, *ACS Sustainable Chem. Eng.*, 2020, **8**, 4948–4954.
35 M. Favaro, H. Xiao, T. Cheng, W. A. Goddard, J. Yano and E. J. Crumlin, *Proc. Natl. Acad. Sci. U. S. A.*, 2017, **114**, 6706–6711.
36 H. Xiao, W. A. Goddard, T. Cheng and Y. Liu, *Proc. Natl. Acad. Sci. U. S. A.*, 2017, **114**, 6685–6688.
37 Q. Lei, H. Zhu, K. Song, N. Wei, L. Liu, D. Zhang, J. Yin, X. Dong, K. Yao and N. Wang, *J. Am. Chem. Soc.*, 2020, **142**, 4213.
38 P. Burroughs, A. Hamnett, A. F. Orchard and G. Thornton, *J. Chem. Soc., Dalton Trans.*, 1976, 1686–1698.
39 Z. Sun, X. Wang, Z. Liu, H. Zhang, P. Yu and L. Mao, *Langmuir*, 2010, **26**, 12383–12389.
40 J. Shyu, K. Otto, W. Watkins, G. Graham, R. Belitz and H. Gandhi, *J. Catal.*, 1988, **114**, 23–33.
41 J. E. Spanier, R. D. Robinson, F. Zhang, S.-W. Chan and I. P. Herman, *Phys. Rev. B: Condens. Matter Mater. Phys.*, 2001, **64**, 245407.
42 H. Hagemann, H. Bill, E. Walker and M. François, *Solid State Commun.*, 1990, **73**, 447–451.
43 M. Li, U. Tumuluri, Z. Wu and S. Dai, *ChemSusChem*, 2015, **8**, 3651–3660.
44 M. Zhang, T. Wu, S. Hong, Q. Fan, Y. Soo, J. Masa, J. Qiu and Z. Sun, *ACS Sustainable Chem. Eng.*, 2019, **7**, 15030–15035.
45 A. Loiudice, P. Lobaccaro, E. A. Kamali, T. Thao, B. H. Huang, J. W. Ager and R. Buonsanti, *Angew. Chem. Int. Ed.*, 2016, **55**, 5789–5792.
46 K. Jiang, R. B. Sandberg, A. J. Akey, X. Liu, D. C. Bell, J. K. Nørskov, K. Chan and H. Wang, *Nat. Catal.*, 2018, **1**, 111–119.
47 C. W. Lee, S.-J. Shin, H. Jung, D. L. T. Nguyen, S. Y. Lee, W. H. Lee, D. H. Won, M. G. Kim, H.-S. Oh and T. Jang, *ACS Energy Lett.*, 2019, **4**, 2241–2248.
48 D. Gao, Y. Zhang, Z. Zhou, F. Cai, X. Zhao, W. Huang, Y. s. Li, J. Zhu, P. Liu and F. Yang, *J. Am. Chem. Soc.*, 2017, **139**, 5652–5655.
49 K. J. P. Schouten, Z. Qin, E. P. Gallent and M. T. M. Koper, *J. Am. Chem. Soc.*, 2012, **134**, 9864–9867.
50 W. Tang, E. Sanville and G. Henkelman, *J. Phys.: Condens. Matter.*, 2009, **21**, 084204.

